

**Evaluation of the response of intracranial xenografts to VEGF signaling inhibition
using multiparametric MRI**

Jessica K.R. Boulton^a, Gary Box^b, Maria Vinci^{b,c}, Lara Perryman^{b,c,1}, Suzanne A. Eccles^b,
Chris Jones^{b,c}, Simon P. Robinson^a

^a Division of Radiotherapy and Imaging, The Institute of Cancer Research, London, SM2 5NG, UK.

^b Division of Cancer Therapeutics, The Institute of Cancer Research, London, SM2 5NG, UK.

^c Division of Molecular Pathology, The Institute of Cancer Research, London, SM2 5NG, UK.

¹ Present Address: Pharmaxis, Frenchs Forest, NSW 2046, Australia.

Email Addresses: Jessica K.R. Boulton: Jessica.Boulton@icr.ac.uk
Gary Box: Gary.Box@icr.ac.uk
Maria Vinci: Maria.Vinci@icr.ac.uk
Lara Perryman: Lara.Perryman@gmail.com
Suzanne A. Eccles: Sue.Eccles@icr.ac.uk
Chris Jones: Chris.Jones@icr.ac.uk
Simon P. Robinson: Simon.Robinson@icr.ac.uk

Corresponding author: Dr Jessica Boulton
Division of Radiotherapy and Imaging
The Institute of Cancer Research,
London
SM2 5NG, UK

Telephone: +44 (0)20 8722 4699

Email: Jessica.Boulton@icr.ac.uk

Abstract

Vascular endothelial growth factor A (VEGF-A), is considered one of the most important factors in tumor angiogenesis, and consequently a number of therapeutics have been developed to inhibit VEGF signalling. Therapeutic strategies to target brain malignancies, both primary brain tumors, particularly in pediatric patients, and metastases, are lacking, but targeting angiogenesis may be a promising approach.

Multiparametric MRI was used to investigate the response of orthotopic SF188^{luc} pediatric glioblastoma xenografts to small molecule pan-VEGFR inhibitor cediranib; and the effects of both cediranib and cross-reactive human/mouse anti-VEGF-A antibody B20-4.1.1 in intracranial MDA-MB-231 LM2-4 breast cancer xenografts over 48 hours.

All therapeutic regimens resulted in significant tumor growth delay. In cediranib-treated SF188^{luc} tumors this was associated with lower K^{trans} (compound biomarker of perfusion and vascular permeability) than in vehicle-treated controls. Cediranib also induced significant reductions in both K^{trans} and apparent diffusion coefficient (ADC) in MDA-MB-231 LM2-4 tumors associated with decreased histologically-assessed perfusion. B20-4.1.1 treatment resulted in decreased K^{trans} but in the absence of a change in perfusion; a non-significant reduction in vascular permeability, assessed by Evans blue extravasation, was observed in treated tumors. The imaging responses of intracranial MDA-MB-231 LM2-4 tumors to VEGF/VEGFR pathway inhibitors with differing mechanisms of action are subtly different.

We show that VEGF pathway blockade resulted in tumor growth retardation and inhibition of tumor vasculature in preclinical models of pediatric glioblastoma and breast cancer brain metastases, suggesting that multiparametric MRI can provide a powerful adjunct to accelerate the development of antiangiogenic therapies for use in these patient populations.

Keywords

Magnetic Resonance Imaging

Vascular Endothelial Growth Factor

Pediatric High Grade Glioma

Brain Metastases

Abbreviations

ADC Apparent diffusion coefficient

DCE-MRI Dynamic contrast-enhanced magnetic resonance imaging

DW-MRI Diffusion-weighted magnetic resonance imaging

fBV Fractional blood volume

H&E Hematoxylin and eosin

IAUGC₆₀ Initial area under the gadolinium concentration curve at 60 seconds

MGE Multi gradient-recalled echo

MRI Magnetic resonance imaging

pHGG Pediatric high grade glioma

TNBC Triple negative breast carcinoma

VEGF Vascular endothelial growth factor

VEGFR Vascular endothelial growth factor receptor

Introduction

Angiogenesis, the development of new blood vessels in order to provide a nutritive blood supply, is considered essential for expansive tumor growth in the brain [1]. Stimulated by the secretion of numerous growth factors by tumor cells, endothelial cells and tumor-associated macrophages [2], angiogenesis in tumors results in structurally irregular vessels that are more tortuous, fragile, dilated and hyper-permeable than normal blood vessels [3]. Vascular endothelial growth factor A (VEGF-A) is considered one of the most important factors in tumor angiogenesis [4]. Consequently a number of therapeutic strategies, including small molecules that inhibit VEGF receptor tyrosine kinase activity (e.g. cediranib) and neutralizing antibodies that specifically bind VEGF-A (e.g. bevacizumab), have been developed [5, 6].

Pediatric high grade gliomas (pHGG) have a very poor clinical outcome, with a median overall survival of 9-18 months [7]; effective treatment strategies are urgently required for these patients. Although it is now clearly recognized that pHGGs have distinct underlying biology compared with histologically similar tumors arising in older adults [8, 9], many key features and pathways are commonly dysregulated. Microvascular endothelial cell proliferation is a key feature of grade IV glioma, glioblastoma, in the WHO classification system, which, along with evidence of necrosis, distinguishes them from grade III tumors, which show evidence of anaplasia and have a high mitotic index. Consequently, with the exception of pilocytic astrocytoma, a highly vascular grade I astrocytoma, tumor vascularity is associated with higher grade [10]. VEGF-A is highly expressed in pediatric brain tumors and is thought to be partly responsible for the loss of blood brain barrier integrity during tumor growth [11].

Brain metastases occur in approximately 30% of patients with breast cancer and are an important cause of cancer morbidity and mortality [12]. Highly proliferative breast tumors, such as those negative for the estrogen, progesterone, and Her2/neu receptors, have enhanced angiogenesis that supports rapid growth and early metastasis, and express high levels of VEGF [13]. Therefore, patients with breast tumors expressing high levels of VEGF may be at a higher risk of developing metastases in the brain, hence antiangiogenic agents may also represent promising agents for the treatment of such tumors.

Magnetic resonance imaging (MRI) enables the visualization of detailed anatomical features with high resolution due to its exquisite soft tissue image contrast, and is the gold standard non-invasive method for the diagnosis, surgical planning and monitoring of brain tumors [14]. However, imaging cannot at present replace biopsy for the accurate histological grading of tumors. Furthermore, advances in functional MRI can provide quantitative biomarkers that inform on biologically relevant structure-function relationships, their heterogeneous distribution, and treatment response/resistance in brain tumors [15, 16]. The Response Assessment in Neuro-Oncology (RANO) guidelines, based on evaluations of adult HGGs, aim to provide more specific and standardized imaging protocols incorporating assessment of non-enhancing components of tumors [17]. The Response Assessment in Pediatric Neuro-Oncology (RAPNO) working group was subsequently established to address the unique challenges associated with pediatric neuro-oncology, for example the more heterogeneous group of diseases arising in children, with a higher prevalence of low grade, infratentorial and brainstem tumors, and the relatively small numbers of cases available for clinical trials [18, 19].

In this study, we undertook a multiparametric MRI approach to investigate the response of orthotopic SF188 pediatric glioblastoma xenografts, and highly malignant MDA-MB-231 LM2-4 human triple negative breast carcinoma (TNBC) xenografts implanted in the brain, to

cediranib, a small molecule pan-VEGFR inhibitor. This approach was also used to assess the effect of B20-4.1.1, a cross-reactive human/mouse derivative of bevacizumab, on intracranial MDA-MB-231 LM2-4 xenografts.

Materials and Methods

Cell Culture

SF188 pediatric glioblastoma cells were maintained in Dulbecco's modified Eagle's medium Hams F12 mixture (Sigma-Aldrich, Gillingham, UK) supplemented with 10% (v/v) fetal bovine serum (Invitrogen, Life Technologies, Paisley, UK) [20]. SF188 cells were engineered to stably express luciferase by transduction with the luc-2 gene (cloned from pGL4.10[luc2] (Promega, Madison, MI)) cloned into pCDH-CMV-CMS-EFI-hygro, a HIV lentiviral-based vector (System Biosciences, Mountain View, CA) and enriched for *in vivo* tumorigenicity via four sequential intracranial passages (SF188^{luc}). Luciferase-expressing MDA-MB-231 LM2-4 highly malignant human TNBC cells isolated from a lung metastasis [21] (provided by Dr. R. Kerbel, University of Toronto, Canada) were maintained in Dulbecco's modified Eagle's medium (Invitrogen, Life Technologies) supplemented with 10% (v/v) fetal bovine serum. Both cell lines were authenticated by short tandem repeat (STR) profiling and tested negative for mycoplasma infection at the time of tumor implantation.

Tumor Implantation

All experiments were performed in accordance with the local Animal Welfare and Ethical Review Board, the UK Home Office Animals (Scientific Procedures) Act 1986, the United Kingdom National Cancer Research Institute guidelines for the welfare of animals in cancer research [22] and the ARRIVE (animal research: reporting *in vivo* experiments) guidelines [23].

SF188^{luc} (2×10^5) or MDA-MB-231 LM2-4 (5×10^3) cells were implanted supratentorially in the brains of 6 week old female athymic (NCr-Foxn1tm) mice (Charles River Ltd, Margate, UK), as previously described [24].

Bioluminescence Imaging

Tumor establishment and growth was monitored using a Xenogen IVIS[®] 200 system coupled with LivingImage software (Caliper Life Sciences, Runcorn, UK). Luciferin (150mg/kg, Caliper Life Sciences) was administered intraperitoneally 10 minutes before imaging. Total photon flux was established for automatically drawn ROIs at a constant threshold. A bioluminescence signal that represented a tumor volume of approximately 25mm³ had previously been established for each cell line; once this signal was reached animals were enrolled in MRI experiments. This starting volume was chosen to provide an experimental timeframe with minimal risk of mice developing adverse neurological symptoms prior to study end.

MRI and Drug Treatment Schedules

Tumor-bearing mice were randomized prior to MRI into control and treatment cohorts as follows:

SF188^{luc}

- i. MRI prior to and after 48h treatment with 6mg/kg cediranib (AZD2171, AstraZeneca) (n=6) or vehicle (1% polysorbate-80 in water) (n=5) daily. 3 oral doses were given over 48h: i) following recovery from anesthesia for pre-treatment imaging, ii) 24h later, iii) a further 24h later immediately prior to post-treatment imaging.

MDA-MB-231 LM2-4

- i. MRI prior to and after 48h treatment with either 6mg/kg cediranib (n=6) or vehicle (n=5), as described above.
- ii. MRI prior to and 48h after a single intraperitoneal 10mg/kg dose of B20-4.1.1 (Genentech) (n=7) or an isotype-matched control antibody (anti-Ragweed:1428) (n=6).

Treatment and imaging regimens are depicted in supplementary Figure S1 with cohort sizes, time from tumor implantation to study start and mean pre-treatment tumor volume.

Magnetic Resonance Imaging (MRI)

Anesthesia was induced with a 10ml/kg intraperitoneal injection of fentanyl citrate (0.315mg/ml) plus fluanisone (10mg/ml (Hypnorm; Janssen Pharmaceutical Ltd. High Wycombe, UK)), midazolam (5mg/ml (Hypnovel; Roche, Burgess Hill, UK)), and sterile water (1:1:2). A lateral tail vein was cannulated with a 27G butterfly catheter (Venisystems, Hospira, Royal Leamington Spa, UK) to enable the remote administration of gadopentetate dimeglumine (Gd-DTPA, Magnevist™; Schering, Berlin, Germany) or ultrasmall paramagnetic iron oxide (USPIO) particles (P904; Guerbet, Villepinte, France). Anesthetized mice were then positioned prone in a 3cm birdcage coil within a 7T Bruker horizontal bore microimaging system (Ettlingen, Germany). Core body temperature was maintained by warm air blown through the magnet bore. All images were acquired over a 2.5cm x 2.5cm field of view.

Anatomical T₂-weighted, Diffusion-Weighted and Dynamic Contrast-Enhanced MRI

Magnetic field homogeneity was optimized by shimming over the entire brain using an automated shimming routine (FASTmap). A rapid acquisition with relaxation enhancement (RARE) T₂-weighted sequence (repetition time (T_R)=4500ms, effective echo time (T_E^{eff})=36ms, 4 averages, RARE factor=8, 256×256 matrix, 20×1mm thick contiguous axial slices) was used for localization of the tumor and measurement of tumor volume. Diffusion-weighted (DW) images were then acquired using an echo-planar imaging (EPI) sequence (T_R=1500ms, T_E=32ms, 10 b-values; b=0, 30, 60, 100, 150, 200, 300, 500, 750, 1000s/mm², 4 averages, 128×128 matrix, 3×1mm thick axial slices through the tumor).

Dynamic contrast-enhanced (DCE) MRI data were acquired using an inversion recovery (IR) true fast imaging with steady-state precession (trueFISP) sequence with one baseline scan ($T_E=1.2\text{ms}$, $T_R=2.4\text{ms}$, scan $T_R=10\text{s}$, 50 inversion times spaced 29ms apart ($T_I=25-1451\text{ms}$), 8 averages, flip angle= 60° , matrix= 128×96 , 1x1mm thick slice) and 60 dynamic scans ($T_E=1.2\text{ms}$, $T_R=2.4\text{ms}$, scan $T_R=10\text{s}$, 8 inversion times spaced 116ms apart ($T_I=109-924\text{ms}$), 1 average, flip angle= 60° , temporal resolution= 20s). A bolus of Gd-DTPA (0.1mmol/kg Magnevist™ i.v., 2ml/kg 50mM solution) was administered at 2ml/minute using a power injector 3 minutes after the start of the dynamic sequence [25].

This imaging protocol was performed in mice bearing SF188^{luc} or MDA-MB-231 tumors at baseline and after 48h treatment with 6mg/kg cediranib, or vehicle, given orally daily, and mice bearing MDA-MB-231 LM2-4 tumors before and 48h following a single intraperitoneal dose of 10mg/kg B20-4.1.1 or isotype control Ragweed:1428 (see supplementary Figure S1).

Susceptibility Contrast MRI

Magnetic field homogeneity was optimized and T_2 -weighted images were acquired. Multi gradient-recalled echo (MGE) images ($T_R=1000\text{ms}$, $T_E=6.2-31.1\text{ms}$, 8 echoes, 2 averages, 256x256 matrix, 3x1mm thick slices) were acquired for quantification of relaxation rate R_2^* . USPIO particles were then administered as a bolus (150 μmol Fe/kg P904 i.v.) and allowed to circulate for two minutes in order to equilibrate before a second set of MGE images were acquired.

This imaging protocol was performed in mice bearing MDA-MB-231 LM2-4 tumors at baseline and after 48h treatment with 6mg/kg cediranib, or vehicle, given orally daily (additional n=5/group; see supplementary Figure S1).

MRI Analysis

Parameter estimation was undertaken using a Bayesian maximum *a posteriori* algorithm, which took into account the Rician distribution of noise in magnitude MR data in order to provide unbiased parameter estimates [26]. Estimates of the apparent diffusion coefficient (ADC), a measure of Brownian water diffusion within tissue and surrogate biomarker of cellularity and edema, were determined from the DW-MRI data (using 5 b-values; 200-1000s/mm²). The dual relaxation rate sensitivity of the IR-trueFISP sequence was utilized, providing estimates of native T₁ and T₂ relaxation times. DCE-MRI data were analysed by incorporating the Tofts and Kermode pharmacokinetic model, from which the volume transfer constant (K^{trans} , minute⁻¹), the rate of flux of contrast agent into the extracellular extravascular space within a given volume, and a compound biomarker of vascular permeability and blood flow, was calculated. In addition, model-free analysis was used to derive the initial area under the gadolinium concentration curve at 60 seconds after injection (IAUGC₆₀, mmol Gd.minute) [25].

Estimates of the MRI transverse relaxation rate R₂* were calculated from MGE data. The change in R₂* following delivery of USPIO (ΔR_2^*) was also evaluated, from which fractional blood volume (fBV, %) was estimated [27]. Voxels corresponding to a fBV exceeding 17% (the limit value for the linearity between ΔR_2^* and fBV) were excluded [28].

All data were fitted on a pixel-by-pixel basis using in-house software (ImageView, developed in IDL, ITT Visual Information Systems, Boulder, CO, USA). The median value of each parameter in each tumor was determined and the distribution of data values was assessed.

Histological Analysis

Tumor bearing mice were administered with 15mg/kg of the perfusion marker Hoechst 33342 (Sigma-Aldrich) intravenously through a lateral tail vein. After 1 minute, animals were killed, and whole brains were rapidly excised, snap-frozen and stored in liquid nitrogen [25].

Hoechst 33342 fluorescence signals from frozen whole brain sections (10 μ m, three per tumor) were recorded at 365nm using a motorized scanning stage (Prior Scientific Instruments, Cambridge, UK) attached to a BX51 microscope (Olympus Optical, London, UK), driven by CellIP (Soft Imaging System, Münster, Germany). In addition, composite images from the tumor region and 40x magnification snapshots of the tumors were acquired.

The same sections were then processed for the detection of vascular endothelial marker CD31 (all tumors) and pan cytokeratin (MDA-MB-231 LM2-4 tumors only). Sections were first incubated with 2% (w/v) BSA/5% (v/v) goat serum in PBS for 1 hour to block any non-specific antibody binding, and then with goat anti-mouse CD31 antibodies (MEC 13.3, BD Biosciences, Oxford, UK, 1:100) overnight at 4°C. Sections were washed with 0.1% (v/v) Tween-20 in PBS, then incubated with Alexa 546-conjugated goat anti-rat secondary antibodies (Invitrogen, 1:500) \pm FITC-conjugated mouse monoclonal anti-pan cytokeratin antibodies (Clone C-11, Sigma-Aldrich, 1:100) at 37°C for 4 hours, protected from light. Following washing the sections were imaged under PBS. CD31 expression was detected at 510-560nm and cytokeratin positive tumor cells were detected over the whole brain at 450-490nm using the same fluorescence microscope system and stage co-ordinates. Composite images of the brain, tumor and individual 40x snapshots were recorded, allowing the CD31 images to be subsequently overlaid on the Hoechst 33342 images. The cytokeratin images were used to draw the MDA-MB-231 LM2-4 tumor regions of interest (ROI) used in the analysis of the Hoechst 33342 and CD31 data.

The sections were then stained with hematoxylin and eosin (H&E), and composite images were acquired using the same microscope system and co-ordinates with bright-field illumination. These images were used to draw the tumor ROIs used in the analysis of the Hoechst 33342 and CD31 data in SF188^{luc} tumors.

Fluorescent particles were detected above a constant threshold and the area of the tumor section with Hoechst 33342 or CD31 fluorescence was determined and expressed as a percentage of the whole tumor section. Co-localization of Hoechst 33342 (perfused vessels) and CD31 (total vessels) was also assessed and expressed as percentage total vessels perfused and a total perfused vessel area.

A separate cohort of mice bearing MDA-MB-231 LM2-4 tumors treated with B20-4.1.1 or isotype-matched control antibodies (n=4/group) were administered intravenously with 50mg/kg Evans blue (Sigma-Aldrich) in PBS. Evans blue readily binds to albumin, and hence can be used to visualize and quantify vascular permeability [29, 30]. After 30 minutes Hoechst 33342 was administered as described above; 1 minute later the animals were killed, and the brains rapidly excised and snap-frozen. Hoechst 33342 and Evans blue fluorescent signals were recorded from frozen sections at 365nm and 510-560nm, respectively. Sections were then blocked with 2% (w/v) BSA/5% (v/v) goat serum in PBS for 1 hour and incubated with FITC-anti-pan cytokeratin antibodies as above. Following washing the sections were imaged under PBS. Fluorescent particles were detected above a constant threshold and the area of the tumor section with Hoechst 33342 or Evans blue fluorescence was determined and expressed as a percentage of the whole tumor section, as determined using cytokeratin staining.

Statistical Analysis

Statistical analysis was performed with GraphPad Prism 7 (GraphPad Software, La Jolla, USA). The mean of median values for all the quantitative MR imaging parameters, and the mean values for tumor volume and the fluorescent area fractions were used for statistical analysis. Results are presented as the mean \pm 1 standard error of the mean (s.e.m.). Significance testing used paired or unpaired Student's t-tests with a 5% confidence level.

Results

Representative anatomical T₂-weighted images, and associated parametric ADC and K^{trans} maps, acquired from mice bearing intracranially implanted SF188^{luc} or MDA-MB-231 LM2-4 tumors, prior to and following treatment with either cediranib, B20-4.1.1, or the appropriate control, are shown in Figures 1, 3 and 5, along with summaries of the quantitative data obtained for each tumor model and treatment regimen investigated. Orthotopic SF188^{luc} tumors presented as moderately homogeneous hyperintense lesions with relatively well defined borders on T₂-weighted MRI images (Figure 1a) and were observed to be well defined masses with sparse foci of infiltrative cells by H&E staining (supplementary Figure S2). Intracranial MDA-MB-231 LM2-4 tumors were more heterogeneous with less well defined boundaries on T₂-weighted images (Figures 3a and 5a), and H&E staining shows partially well circumscribed masses with substantial local invasion, principally occurring along blood vessels, with evidence of edema (supplementary Figure S2) [16, 24].

Treatment of mice bearing orthotopic SF188^{luc} pediatric glioblastomas with cediranib significantly inhibited tumor progression compared with vehicle-treated controls ($p < 0.01$, Figure 1a&b). Tumor ADC was not significantly altered over 48 hours in either treatment group (Figure 1b). In the cediranib-treated SF188^{luc} cohort DCE-MRI consistently showed a marked reduction in contrast agent uptake after treatment, resulting in non-significant 53% and 59% reductions in K^{trans} (Figure 1b) and IAUGC₆₀ (data not shown), respectively. The mean post-treatment K^{trans} was significantly lower in the cediranib-treated cohort than in the vehicle-treated controls ($p < 0.05$). Frequency histograms of individual voxel ADC and K^{trans} values in five equally sized bins were also used to evaluate any treatment-induced changes in data distribution (Figure 1c). Differences in the distribution of K^{trans} values prior to and following treatment with cediranib were apparent, including a marked increase in the

proportion of voxels with values of $0-0.02\text{min}^{-1}$ and a significant reduction in values of $0.02-0.04\text{min}^{-1}$ ($p<0.05$). Histological assessment of Hoechst 33342 perfused area, CD31 positive total vessel area, and their co-localization in SF188^{luc} tumors treated with either vehicle or cediranib revealed no significant difference in vascular perfusion, total vascular area or the percentage of vessels perfused at the time of Hoechst 33342 injection between treatment groups (Figure 2).

Treatment of intracranially-implanted MDA-MB-231 LM2-4 tumors with cediranib resulted in significant growth delay compared with vehicle-treated controls ($p<0.05$, Figure 3a&b). This response was associated with a statistically significant 9% reduction in ADC in the cediranib-treated cohort ($p<0.05$), accompanied by significant 49% and 52% decreases in K^{trans} (Figure 3b) and IAUGC₆₀ (data not shown), respectively ($p<0.05$). There was no significant change in DW- or DCE-MRI parameters over 48h in the vehicle-treated cohort. Frequency histograms showed that the reduction in ADC following cediranib treatment was associated with a decrease in the proportion of voxels with values of $900-1200 \times 10^{-6} \text{mm}^2 \text{s}^{-1}$ ($p<0.05$) and $1200-1500 \times 10^{-6} \text{mm}^2 \text{s}^{-1}$ ($p=0.08$), and increases in the number of voxels in the $300-600$ and $600-900 \times 10^{-6} \text{mm}^2 \text{s}^{-1}$ bins ($p=0.08$) (Figure 3c). The reduction in K^{trans} in the cediranib-treated tumors was associated with a non-significant increase in the proportion of voxel values of $0-0.2\text{min}^{-1}$ and reductions in the size in all other bins. Histological assessment of Hoechst 33342 uptake demonstrated that cediranib-treated MDA-MB-231 LM2-4 tumors were significantly less well perfused than vehicle-treated tumors ($p<0.05$, Figure 4). CD31 positive total vessel area was also lower in the treated tumors, but the difference did not reach statistical significance ($p=0.052$). Assessment of the co-localization of Hoechst 33342 and CD31 revealed that the percentage of vessels perfused at the time of Hoechst 33342 injection was significantly lower in the cediranib-treated cohort ($p<0.05$). Susceptibility contrast MRI revealed no significant treatment-induced change in the fractional

blood volume (fBV) of the MDA-MB-231 LM2-4 tumors (pre vehicle $5.0\pm 0.4\%$, 48h vehicle $4.7\pm 0.1\%$; pre cediranib $5.1\pm 0.3\%$, 48h cediranib $5.1\pm 0.4\%$).

Treatment with a single dose of B20-4.1.1 significantly inhibited the growth of intracranial MDA-MB-231 LM2-4 tumors over 48 hours compared with controls ($p < 0.01$, Figure 5a&b). There was no significant change in ADC in the B20-4.1.1-treated tumors but growth inhibition was associated with significant 41% and 53% reductions in K^{trans} (Figure 5b) and IAUGC₆₀ (data not shown), respectively ($p < 0.05$). No quantitative MRI parameters changed over 48 hours in the control tumors. Despite there being no significant change in overall tumor ADC in response to B20-4.1.1, a change in the distribution of the data was apparent, with a significant reduction in the proportion of voxels with ADC values of $900-1200 \times 10^{-6} \text{mm}^2 \text{sec}^{-1}$ and a significant increase in voxels with values of $300-600 \times 10^{-6} \text{mm}^2 \text{sec}^{-1}$ (both $p < 0.05$). The reduction in K^{trans} in the B20-4.1.1-treated cohort was attributable to a significant increase in the number of voxels with a value of $0-0.02 \text{min}^{-1}$ and significant reductions the proportion of voxels with values between $0.2-0.4 \text{min}^{-1}$ and $0.4-0.6 \text{min}^{-1}$ (all $p < 0.05$, Figure 5c). Histological assessment of Hoechst 33342 uptake, CD31 expression and their co-localization in MDA-MB-231 LM2-4 tumors treated with either B20-4.1.1 or control antibodies revealed no difference in vascular perfusion (Figure 6), total vascular area or the percentage of perfused vessels between treatment groups (data not shown). A markedly lower uptake and distribution of the permeability marker Evans Blue was apparent in the B20-4.1.1-treated tumors compared with the control cohort (B20-4.1.1 $22\pm 5\%$, control $34\pm 2\%$, $p = 0.068$).

Discussion

In this study multiparametric MRI was used to assess the response of intracranial tumors to drugs targeting the VEGF/VEGFR pathway. Specifically, the efficacy of the pan-VEGFR small molecule inhibitor cediranib in orthotopic SF188^{luc} pediatric glioblastoma xenografts and intracranial MDA-MB-231 LM2-4 TNBC xenografts was assessed alongside the response of MDA-MB-231 LM2-4 tumors to the human/mouse cross-reactive anti-VEGF-A monoclonal antibody B20-4.1.1. Anatomical T₂-weighted MRI and functional DW- and DCE-MRI were used to assess any treatment-induced changes in tumor progression, cellularity and edema, and vascular permeability/perfusion, respectively. An acute time point of 48h was chosen because early imaging changes have been detected in glioblastoma, breast cancer and other solid tumors, including extracranial breast cancer metastases, following cediranib, bevacizumab and axitinib treatment [15, 31, 32]. In addition, response to bevacizumab at just 96h, as well as 4 weeks, was predictive of improved PFS in recurrent glioma [33].

Treatment of orthotopic SF188^{luc} pediatric glioblastoma xenografts with cediranib resulted in significant growth delay over 48 hours. DW-MRI revealed no significant change in water diffusivity following treatment with cediranib in SF188^{luc} tumors; these tumors were densely cellular and there was no edema present (supplementary Figure S2), exemplified by baseline ADC values being considerably lower in SF188^{luc} than MDA-MB-231 LM2-4 tumors (mean pre-treatment ADC; SF188^{luc} $621 \times 10^{-6} \text{mm}^2 \text{s}^{-1}$, MDA-MB-231 LM2-4 $827 \times 10^{-6} \text{mm}^2 \text{s}^{-1}$). Paired comparisons of mean DCE-MRI data acquired from the same tumors prior to and post treatment did not reveal any significant anti-vascular effect. However, assessment of the distribution of K^{trans} values revealed a shift towards lower values in the treated tumors. The lack of an overall significant response is likely a consequence of the wide dynamic range of

pre-treatment K^{trans} values measured in the cediranib-treated group. The average post-treatment K^{trans} was, however, significantly lower in the cohort treated with cediranib compared with the vehicle-treated tumors, suggestive of an anti-vascular effect.

Adult patients with glioblastoma treated with bevacizumab, alone or in combination with chemotherapy (most commonly irinotecan), have demonstrated reductions in MRI contrast enhancement and vasogenic edema resulting in significant improvements in progression-free survival [15, 34]. Bevacizumab in combination with radiotherapy and temozolomide has also been shown to extend progression free survival in newly diagnosed glioblastoma [35, 36]. A phase I clinical trial assessing cediranib as a single agent in children with recurrent and refractory primary central nervous system tumors has recently been completed, in which decreased diffusivity and perfusion were observed in responding tumours [37]. The efficacy of bevacizumab in combination with chemotherapy or radiotherapy is currently being assessed in the same patient population [38], with functional MRI included in at least one such trial [19].

Growth of intracranial MDA-MB-231 LM2-4 tumors was significantly suppressed over the duration of 48 hours treatment with cediranib. The sensitivity of the parental MDA-MB-231 cell line to cediranib has previously been shown *in vitro* and *in vivo* in subcutaneous xenografts [5]. Here, cediranib-induced growth delay in intracranial MDA-MB-231 LM2-4 tumors was associated with significant reductions in both K^{trans} , measured *in vivo* by DCE-MRI, and perfused vessel area assessed histologically. Interestingly, susceptibility contrast MRI using an intravascular USPIO particle-based contrast agent revealed no significant difference in tumor fractional blood volume (fBV) in response to cediranib. Contrary to gadolinium-chelated contrast agents such as Magnevist, high molecular weight USPIO particles do not leak as readily from the blood vessels, hence quantitation of fBV represents an imaging biomarker of more patent vasculature. The differential response of K^{trans} and fBV

observed herein therefore suggests that cediranib is targeting permeable neovasculature in the intracranial MDA-MB-231 LM2-4 tumors. Indeed, previous studies of anti-VEGF therapeutics have shown that the reduction in K^{trans} is associated with pruning of immature vessels [15]. Treatment with cediranib also elicited a significant reduction in tumor ADC, consistent with the resolution of edema following pruning of hyperpermeable vessels and the resulting reduction in fluid extravasation; which has been observed in both preclinical models of glioblastoma and patients with brain tumors [15, 39]. The reduction in edema, and therefore intracranial pressure, is thought to have a significant role in increased survival following VEGF blockade [15, 39].

Cediranib is primarily a potent pan-VEGFR inhibitor, but at the dose used in this study also elicits marked activity against c-kit and platelet-derived growth factor receptor (PDGFR)- α and - β [40], whose inhibition may also contribute to the anti-tumor and anti-vascular effects observed. Amplification of *PDGFRA*, and less commonly *PDGFRB*, is observed in pediatric high grade glioma [41-43], indeed SF188^{luc} cells overexpress PDGFR β [44]. Overexpression of PDGFR α is also an adverse prognostic factor in advanced breast cancer [45, 46].

MDA-MB-231 LM2-4 tumors were also treated with B20-4.1.1, a cross-reactive human/mouse anti-VEGF-A monoclonal antibody, that allows the simultaneous targeting of VEGF-A produced by human-derived tumor cells and mouse-derived stromal cells. Whilst the relative contributions of tumor- and stroma- derived VEGF-A differ between *in vivo* tumor models [47], targeting both recapitulates patient response more accurately than targeting tumor-derived VEGF alone. Similar to the response following treatment with cediranib, B20-4.1.1 elicited significant growth delay in MDA-MB-231 LM2-4 tumors relative to isotype-matched antibody-treated mice. Treatment with B20-4.1.1 also resulted in a significant reduction in K^{trans} . This was however not associated with a reduction in Hoechst 33342 perfusion, total CD31 positive vessel area or percentage of vessels perfused,

suggesting that the change in K^{trans} may predominantly reflect a reduction in vascular permeability. The uptake of Evans blue, an azo dye with high affinity for albumin used to assess the degree of tumor vascular permeability, and unable to pass through the blood brain barrier, was lower in B20.4.1.1-treated tumors, but values did not reach statistical significance. Whilst the mean of individual tumor median ADC values did not change in response to treatment with B20-4.1.1, a change in the distribution of the data, with a shift towards lower values, was observed, suggesting some alteration in the degree of water diffusion with the tumors post treatment, again possibly as a result of resolution of edema.

The imaging response of intracranial MDA-MB-231 LM2-4 tumors to VEGF/VEGFR pathway inhibitors with differing mechanisms of action are subtly different, with perfused vessel area and degree of water diffusion not significantly changing in response to B20-4.1.1, but being altered by cediranib treatment.

In a recent phase II study, patients with parenchymal brain breast metastases who responded to bevacizumab in combination with carboplatin demonstrated improved cerebral blood flow, pruning of macroscopic vessels and increased oxygen saturation as a result of vascular normalization [48]. Reduced tumor vessel perfusion/permeability has also been observed following bevacizumab treatment in previously untreated patients with inflammatory or locally advanced breast cancer [31].

SF188^{luc} tumors grow as well defined masses with sparse foci of infiltrative cells, therefore not accurately modelling the heterogeneity of pHGG growth with infiltrative regions, however these tumors model the angiogenic component of the tumors that VEGF pathway inhibition targets. Similarly, whilst intracranial implantation of MDA-MB-231 LM2-4 cells does not strictly model brain breast cancer metastasis, these tumors grow as partially well circumscribed, partially invasive, tumors with lower vascular permeability in invasive regions

[16] and provide a reproducible model of intracranial tumor growth in which to perform imaging investigations.

The vascular and diffusion parameters reported herein did not change in any control cohort, all of which exhibited a larger change in volume over 48h than the treated tumors, demonstrating that these biomarkers are not affected by tumor volume over this size range.

DCE-MRI-derived estimates of K^{trans} using a low molecular weight gadolinium-chelated contrast agents represents a compound biomarker of both tumor perfusion and permeability [49], and changes in K^{trans} in response to vascular-targeted therapies can be challenging to correctly interpret [50]; VEGF pathway blockade has been shown to partially restore the compromised blood brain barrier in human glioblastomas resulting in reduced tumor detectability by Gd-DTPA enhanced MRI [51]. In DCE-MRI studies of human brain tumors, K^{trans} is often reported as a measure of permeability alone, due to the high flow rate and low permeability of brain blood vessels [52]. Alternative imaging strategies are therefore continually being evaluated for the assessment of brain tumor perfusion and its response *in vivo* [53, 54]. Dynamic susceptibility MRI, acquired during the first circulatory pass of Gd-DTPA, can provide a measure of cerebral blood flow (CBF, ml/100g/min), which has been reported to decrease in response to cediranib in glioma patients [15].

We show here that in preclinical models of pediatric glioblastoma and breast cancer brain metastases VEGF pathway blockade resulted in tumor growth retardation and inhibition of tumor vasculature. These data suggest that antiangiogenic therapy, alone or in combination, may be beneficial and is worth pursuing in patients with brain metastases and in pediatric brain tumor patients, both of which are patient populations with limited therapeutic options.

The use of multiparametric MRI to monitor such regimens may also inform on expedient therapy switching in the event of poor response and may provide a powerful adjunct to

accelerate the development of new antiangiogenic therapies for use in these patient populations.

Acknowledgements

We acknowledge the CRUK and EPSRC support to the Cancer Imaging Centre at The Institute of Cancer Research and The Royal Marsden Hospital in association with the MRC and Department of Health (England) [grant numbers C1060/A10334, C1060/A16464], CRUK funding to the Cancer Therapeutics Unit [grant number C309/A11566], and NHS funding to the NIHR Biomedical Research Centre at The Royal Marsden and the ICR. We thank Allan Thornhill and his staff for animal maintenance, AstraZeneca (Macclesfield, UK) for supplying cediranib (AZD2171) and Genentech, Inc. (San Francisco, USA) for supplying B20-4.1.1 and isotype control Ragweed:1428.

References

- [1] Fischer I, Gagner JP, Law M, Newcomb EW, Zagzag D (2005). Angiogenesis in gliomas: biology and molecular pathophysiology. *Brain Pathol* **15**, 297-310.
- [2] Yancopoulos GD, Davis S, Gale NW, Rudge JS, Wiegand SJ, Holash J (2000). Vascular-specific growth factors and blood vessel formation. *Nature* **407**, 242-248. 10.1038/35025215.
- [3] Yuan F, Salehi HA, Boucher Y, Vasthare US, Tuma RF, Jain RK (1994). Vascular permeability and microcirculation of gliomas and mammary carcinomas transplanted in rat and mouse cranial windows. *Cancer Res* **54**, 4564-4568.
- [4] Ferrara N (2002). VEGF and the quest for tumour angiogenesis factors. *Nat Rev Cancer* **2**, 795-803. 10.1038/nrc909.
- [5] Wedge SR, Kendrew J, Hennequin LF, Valentine PJ, Barry ST, Brave SR, Smith NR, James NH, Dukes M, Curwen JO, et al. (2005). AZD2171: a highly potent, orally bioavailable, vascular endothelial growth factor receptor-2 tyrosine kinase inhibitor for the treatment of cancer. *Cancer Res* **65**, 4389-4400. 10.1158/0008-5472.CAN-04-4409.
- [6] Ferrara N, Hillan KJ, Gerber HP, Novotny W (2004). Discovery and development of bevacizumab, an anti-VEGF antibody for treating cancer. *Nat Rev Drug Discov* **3**, 391-400. 10.1038/nrd1381.
- [7] Jones C, Perryman L, Hargrave D (2012). Paediatric and adult malignant glioma: close relatives or distant cousins? *Nat Rev Clin Oncol* **9**, 400-413. 10.1038/nrclinonc.2012.87.
- [8] Jones C, Baker SJ (2014). Unique genetic and epigenetic mechanisms driving paediatric diffuse high-grade glioma. *Nat Rev Cancer* **14**, 651-661. 10.1038/nrc3811.
- [9] Sturm D, Bender S, Jones DT, Lichter P, Grill J, Becher O, Hawkins C, Majewski J, Jones C, Costello JF, et al. (2014). Paediatric and adult glioblastoma: multifactorial (epi)genomic culprits emerge. *Nat Rev Cancer* **14**, 92-107. 10.1038/nrc3655.
- [10] Louis DN, Ohgaki H, Wiestler OD, Cavenee WK, Burger PC, Jouvet A, Scheithauer BW, Kleihues P (2007). The 2007 WHO classification of tumours of the central nervous system. *Acta Neuropathol* **114**, 97-109. 10.1007/s00401-007-0243-4.
- [11] Sie M, den Dunnen WF, Hoving EW, de Bont ES (2014). Anti-angiogenic therapy in pediatric brain tumors: an effective strategy? *Crit Rev Oncol Hematol* **89**, 418-432. 10.1016/j.critrevonc.2013.09.005.
- [12] Arshad F, Wang L, Sy C, Avraham S, Avraham HK (2010). Blood-brain barrier integrity and breast cancer metastasis to the brain. *Patholog Res Int* **2011**, 920509. 10.4061/2011/920509.

- [13] Hu Z, Fan C, Livasy C, He X, Oh DS, Ewend MG, Carey LA, Subramanian S, West R, Ikpatt F, et al. (2009). A compact VEGF signature associated with distant metastases and poor outcomes. *BMC Med* **7**, 9. 10.1186/1741-7015-7-9.
- [14] Rees JH (2011). Diagnosis and treatment in neuro-oncology: an oncological perspective. *Br J Radiol* **84 Spec No 2**, S82-89. 10.1259/bjr/18061999.
- [15] Batchelor T, Sorensen A, di Tomaso E, Zhang W, Duda D, Cohen K, Kozak K, Cahill D, Chen P, Zhu M, et al. (2007). AZD2171, a pan-VEGF receptor tyrosine kinase inhibitor, normalizes tumor vasculature and alleviates edema in glioblastoma patients. *Cancer Cell* **11**, 83-95. 10.1016/j.ccr.2006.11.021.
- [16] Boulton JK, Borri M, Jury A, Popov S, Box G, Perryman L, Eccles SA, Jones C, Robinson SP (2016). Investigating intracranial tumour growth patterns with multiparametric MRI incorporating Gd-DTPA and USPIO-enhanced imaging. *NMR Biomed* **29**, 1608-1617. 10.1002/nbm.3594.
- [17] Wen PY, Macdonald DR, Reardon DA, Cloughesy TF, Sorensen AG, Galanis E, Degroot J, Wick W, Gilbert MR, Lassman AB, et al. (2010). Updated response assessment criteria for high-grade gliomas: response assessment in neuro-oncology working group. *J Clin Oncol* **28**, 1963-1972. 10.1200/JCO.2009.26.3541.
- [18] Warren KE, Poussaint TY, Vezina G, Hargrave D, Packer RJ, Goldman S, Wen PY, Pollack IF, Zurakowski D, Kun LE, et al. (2013). Challenges with defining response to antitumor agents in pediatric neuro-oncology: a report from the response assessment in pediatric neuro-oncology (RAPNO) working group. *Pediatr Blood Cancer* **60**, 1397-1401. 10.1002/pbc.24562.
- [19] Jaspan T, Morgan PS, Warmuth-Metz M, Sanchez Aliaga E, Warren D, Calmon R, Grill J, Hargrave D, Garcia J, Zahlmann G (2016). Response Assessment in Pediatric Neuro-Oncology: Implementation and Expansion of the RANO Criteria in a Randomized Phase II Trial of Pediatric Patients with Newly Diagnosed High-Grade Gliomas. *Am J Neuroradiol* **37**, 1581-1587. 10.3174/ajnr.A4782.
- [20] Bax DA, Little SE, Gaspar N, Perryman L, Marshall L, Viana-Pereira M, Jones TA, Williams RD, Grigoriadis A, Vassal G, et al. (2009). Molecular and phenotypic characterisation of paediatric glioma cell lines as models for preclinical drug development. *PLoS One* **4**, e5209. 10.1371/journal.pone.0005209.
- [21] Munoz R, Man S, Shaked Y, Lee CR, Wong J, Francia G, Kerbel RS (2006). Highly efficacious nontoxic preclinical treatment for advanced metastatic breast cancer using combination oral UFT-cyclophosphamide metronomic chemotherapy. *Cancer Res* **66**, 3386-3391. 10.1158/0008-5472.CAN-05-4411.
- [22] Workman P, Aboagye E, Balkwill F, Balmain A, Bruder G, Chaplin D, Double J, Everitt J, Farningham D, Glennie M, et al. (2010). Guidelines for the welfare and use of animals in cancer research. *Br J Cancer* **102**, 1555-1577. 10.1038/sj.bjc.6605642.

- [23] Kilkenney C, Browne WJ, Cuthill IC, Emerson M, Altman DG (2010). Improving bioscience research reporting: the ARRIVE guidelines for reporting animal research. *PLoS Biol* **8**, e1000412. 10.1371/journal.pbio.1000412.
- [24] Jamin Y, Boulton JK, Li J, Popov S, Garteiser P, Ulloa JL, Cummings C, Box G, Eccles SA, Jones C, et al. (2015). Exploring the biomechanical properties of brain malignancies and their pathologic determinants in vivo with magnetic resonance elastography. *Cancer Res* **75**, 1216-1224. 10.1158/0008-5472.CAN-14-1997.
- [25] Boulton JK, Walker-Samuel S, Jamin Y, Leiper JM, Whitley GS, Robinson SP (2011). Active site mutant dimethylarginine dimethylaminohydrolase 1 expression confers an intermediate tumour phenotype in C6 gliomas. *J Pathol* **225**, 344-352. 10.1002/path.2904.
- [26] Walker-Samuel S, Orton M, McPhail LD, Boulton JK, Box G, Eccles SA, Robinson SP (2010). Bayesian estimation of changes in transverse relaxation rates. *Magn Reson Med* **64**, 914-921. 10.1002/mrm.22478.
- [27] Yablonskiy DA, Haacke EM (1994). Theory of NMR signal behavior in magnetically inhomogeneous tissues: the static dephasing regime. *Magn Reson Med* **32**, 749-763.
- [28] Troprès I, Lamalle L, Péoc'h M, Farion R, Usson Y, Décorps M, Rémy C (2004). In vivo assessment of tumoral angiogenesis. *Magn Reson Med* **51**, 533-541. 10.1002/mrm.20017.
- [29] Rawson RA (1943). The Binding of T-1824 and Structurally Related Diazo Dyes by the Plasma Proteins. *Am J Physiol* **138**, 708-717.
- [30] Schnell CR, Stauffer F, Allegrini PR, O'Reilly T, McSheehy PM, Dartois C, Stumm M, Cozens R, Littlewood-Evans A, Garcia-Echeverria C, et al. (2008). Effects of the dual phosphatidylinositol 3-kinase/mammalian target of rapamycin inhibitor NVP-BEZ235 on the tumor vasculature: implications for clinical imaging. *Cancer Res* **68**, 6598-6607. 10.1158/0008-5472.CAN-08-1044.
- [31] Wedam SB, Low JA, Yang SX, Chow CK, Choyke P, Danforth D, Hewitt SM, Berman A, Steinberg SM, Liewehr DJ, et al. (2006). Antiangiogenic and antitumor effects of bevacizumab in patients with inflammatory and locally advanced breast cancer. *J Clin Oncol* **24**, 769-777. 10.1200/JCO.2005.03.4645.
- [32] Liu G, Rugo HS, Wilding G, McShane TM, Evelhoch JL, Ng C, Jackson E, Kelcz F, Yeh BM, Lee FT, Jr., et al. (2005). Dynamic contrast-enhanced magnetic resonance imaging as a pharmacodynamic measure of response after acute dosing of AG-013736, an oral angiogenesis inhibitor, in patients with advanced solid tumors: results from a phase I study. *J Clin Oncol* **23**, 5464-5473. 10.1200/JCO.2005.04.143.
- [33] Kreisl TN, Kim L, Moore K, Duic P, Royce C, Stroud I, Garren N, Mackey M, Butman JA, Camphausen K, et al. (2009). Phase II trial of single-agent bevacizumab followed by bevacizumab plus irinotecan at tumor progression in recurrent glioblastoma. *J Clin Oncol* **27**, 740-745. 10.1200/JCO.2008.16.3055.

- [34] Chamberlain MC (2011). Bevacizumab for the treatment of recurrent glioblastoma. *Clin Med Insights Oncol* **5**, 117-129. 10.4137/CMO.S7232.
- [35] Gilbert MR, Dignam JJ, Armstrong TS, Wefel JS, Blumenthal DT, Vogelbaum MA, Colman H, Chakravarti A, Pugh S, Won M, et al. (2014). A randomized trial of bevacizumab for newly diagnosed glioblastoma. *N Engl J Med* **370**, 699-708. 10.1056/NEJMoa1308573.
- [36] Chinot OL, Wick W, Mason W, Henriksson R, Saran F, Nishikawa R, Carpentier AF, Hoang-Xuan K, Kavan P, Cernea D, et al. (2014). Bevacizumab plus radiotherapy-temozolomide for newly diagnosed glioblastoma. *N Engl J Med* **370**, 709-722. 10.1056/NEJMoa1308345.
- [37] Kieran MW, Chi S, Goldman S, Onar-Thomas A, Poussaint TY, Vajapeyam S, Fahey F, Wu S, Turner DC, Stewart CF, et al. (2015). A phase I trial and PK study of cediranib (AZD2171), an orally bioavailable pan-VEGFR inhibitor, in children with recurrent or refractory primary CNS tumors. *Childs Nerv Syst* **31**, 1433-1445. 10.1007/s00381-015-2812-5.
- [38] ClinicalTrials.gov.
<https://clinicaltrials.gov/ct2/results?term=avastin+brain+childhood&Search=Search>.
Health USNIo. 9th March 2017.
- [39] Kamoun W, Ley C, Farrar C, Duyverman A, Lahdenranta J, Lacorre D, Batchelor T, di Tomaso E, Duda D, Munn L, et al. (2009). Edema control by cediranib, a vascular endothelial growth factor receptor-targeted kinase inhibitor, prolongs survival despite persistent brain tumor growth in mice. *J Clin Oncol* **27**, 2542-2552. 10.1200/JCO.2008.19.9356.
- [40] Brave SR, Ratcliffe K, Wilson Z, James NH, Ashton S, Wainwright A, Kendrew J, Dudley P, Broadbent N, Sproat G, et al. (2011). Assessing the activity of cediranib, a VEGFR-2/3 tyrosine kinase inhibitor, against VEGFR-1 and members of the structurally related PDGFR family. *Mol Cancer Ther* **10**, 861-873. 10.1158/1535-7163.MCT-10-0976.
- [41] Becher OJ, Hambarzumyan D, Walker TR, Helmy K, Nazarian J, Albrecht S, Hiner RL, Gall S, Huse JT, Jabado N, et al. (2010). Preclinical evaluation of radiation and perifosine in a genetically and histologically accurate model of brainstem glioma. *Cancer Res* **70**, 2548-2557. 10.1158/0008-5472.CAN-09-2503.
- [42] Paugh BS, Qu C, Jones C, Liu Z, Adamowicz-Brice M, Zhang J, Bax DA, Coyle B, Barrow J, Hargrave D, et al. (2010). Integrated molecular genetic profiling of pediatric high-grade gliomas reveals key differences with the adult disease. *J Clin Oncol* **28**, 3061-3068. 10.1200/JCO.2009.26.7252.
- [43] Bax DA, Mackay A, Little SE, Carvalho D, Viana-Pereira M, Tamber N, Grigoriadis AE, Ashworth A, Reis RM, Ellison DW, et al. (2010). A distinct spectrum of copy number aberrations in pediatric high-grade gliomas. *Clin Cancer Res* **16**, 3368-3377. 10.1158/1078-0432.CCR-10-0438.

- [44] Bielen A, Perryman L, Box GM, Valenti M, de Haven Brandon A, Martins V, Jury A, Popov S, Gowan S, Jeay S, et al. (2011). Enhanced efficacy of IGF1R inhibition in pediatric glioblastoma by combinatorial targeting of PDGFRalpha/beta. *Mol Cancer Ther* **10**, 1407-1418. 10.1158/1535-7163.MCT-11-0205.
- [45] Anan K, Morisaki T, Katano M, Ikubo A, Kitsuki H, Uchiyama A, Kuroki S, Tanaka M, Torisu M (1996). Vascular endothelial growth factor and platelet-derived growth factor are potential angiogenic and metastatic factors in human breast cancer. *Surgery* **119**, 333-339.
- [46] Seymour L, Bezwoda WR (1994). Positive immunostaining for platelet derived growth factor (PDGF) is an adverse prognostic factor in patients with advanced breast cancer. *Breast Cancer Res Treat* **32**, 229-233.
- [47] Liang WC, Wu X, Peale FV, Lee CV, Meng YG, Gutierrez J, Fu L, Malik AK, Gerber HP, Ferrara N, et al. (2006). Cross-species vascular endothelial growth factor (VEGF)-blocking antibodies completely inhibit the growth of human tumor xenografts and measure the contribution of stromal VEGF. *J Biol Chem* **281**, 951-961. 10.1074/jbc.M508199200.
- [48] Emblem K, Pinho M, Chandra V, Gerstner E, Stufflebeam S, Sorenson G, Harris G, Freedman R, Sohl J, Younger J, et al. (2014). Brain Breast Metastases Respond to Anti-Angiogenic Therapy by Modes of Vascular Normalization. *Neuro Oncol* **16**, v143. 10.1093/neuonc/nou264.22.
- [49] Leach M, Brindle K, Evelhoch J, Griffiths J, Horsman M, Jackson A, Jayson G, Judson I, Knopp M, Maxwell R, et al. (2005). The assessment of antiangiogenic and antivascular therapies in early-stage clinical trials using magnetic resonance imaging: issues and recommendations. *Br J Cancer* **92**, 1599-1610. 10.1038/sj.bjc.6602550.
- [50] Baker LC, Boulton JK, Thomas M, Koehler A, Nayak T, Tessier J, Ooi CH, Birzele F, Belousov A, Zajac M, et al. (2016). Acute tumour response to a bispecific Ang-2-VEGF-A antibody: insights from multiparametric MRI and gene expression profiling. *Br J Cancer* **115**, 691-702. 10.1038/bjc.2016.236.
- [51] Sorensen AG, Batchelor TT, Zhang WT, Chen PJ, Yeo P, Wang M, Jennings D, Wen PY, Lahdenranta J, Ancukiewicz M, et al. (2009). A "vascular normalization index" as potential mechanistic biomarker to predict survival after a single dose of cediranib in recurrent glioblastoma patients. *Cancer Res* **69**, 5296-5300. 10.1158/0008-5472.CAN-09-0814.
- [52] Jackson A, Jayson GC, Li KL, Zhu XP, Checkley DR, Tessier JJ, Waterton JC (2003). Reproducibility of quantitative dynamic contrast-enhanced MRI in newly presenting glioma. *Br J Radiol* **76**, 153-162. 10.1259/bjr/70653746.
- [53] Gahramanov S, Varallyay C, Tyson RM, Lacy C, Fu R, Netto JP, Nasser M, White T, Woltjer RL, Gultekin SH, et al. (2014). Diagnosis of pseudoprogression using MRI perfusion in patients with glioblastoma multiforme may predict improved survival. *CNS Oncol* **3**, 389-400. 10.2217/cns.14.42.

- [54] Emblem KE, Mouridsen K, Bjornerud A, Farrar CT, Jennings D, Borra RJ, Wen PY, Ivy P, Batchelor TT, Rosen BR, et al. (2013). Vessel architectural imaging identifies cancer patient responders to anti-angiogenic therapy. *Nat Med* **19**, 1178-1183. [10.1038/nm.3289](https://doi.org/10.1038/nm.3289).

Figure Legends

Figure 1. Anatomical, diffusion-weighted and dynamic contrast-enhanced MRI of orthotopic SF188^{luc} tumors treated with cediranib.

a) T₂-weighted MRI images, and associated parametric apparent diffusion coefficient (ADC) and K^{trans} maps, from representative orthotopic SF188^{luc} pediatric glioblastomas prior to and following 48 hours treatment with either vehicle or cediranib, as indicated. **b)** Quantification of the change in tumor volume over the 48h treatment period, and of ADC and K^{trans} prior to, and following, treatment with vehicle (n=5) or cediranib (n=6). **c)** Frequency distributions of all tumor ADC and K^{trans} voxels. Distributions were divided into 5 equally sized bins for each dataset, using 0-300, 300-600, 600-900, 900-1200, 1200-1500x10⁻⁶mm²sec⁻¹ for ADC and 0-0.2, 0.2-0.4, 0.4-0.6, 0.6-0.8, 0.8-0.1min⁻¹ for K^{trans} . ##p<0.01, #p<0.05, unpaired Student's t-test between vehicle and cediranib-treated cohorts. *p<0.05, paired Student's t-test.

Figure 2. Histological assessment of perfusion and vascular density in orthotopic SF188^{luc} tumors in response to cediranib.

a) Representative fluorescence images of the uptake of the perfusion marker Hoechst 33342 (blue), and immunohistochemical detection of the vascular endothelial marker CD31 (red), acquired from whole brain sections from mice bearing orthotopic SF188^{luc} tumors treated with vehicle or cediranib. Composite Hoechst 33342 and CD31 images acquired at 40x magnification are also shown, demonstrating both co-localisation and mismatch of the vascular markers. Tumor ROIs are shown in green, T denotes tumor region on the composite images. **b)** Quantification of Hoechst 33342 perfused area, CD31 positive vessel area, and the percentage of vessels perfused. Three sections per tumor were assessed and the mean for each tumor is represented.

Figure 3. Anatomical, diffusion-weighted and dynamic contrast-enhanced MRI of intracranial MDA-MB-231 LM2-4 tumors treated with cediranib.

a) T₂-weighted MRI images, and associated parametric ADC and K^{trans} maps, from representative intracranial MDA-MB-231 LM2-4 tumors prior to, and following, 48 hours treatment with either vehicle or 6mg/kg cediranib daily, as indicated. b) Quantification of the change in tumor volume over the 48h treatment period, and of ADC and K^{trans} prior to, and following, treatment with either vehicle (n=5) or cediranib (n=6). c) Frequency distributions of all tumor ADC and K^{trans} voxels. Distributions were divided into 5 equally sized bins for each dataset, using 0-300, 300-600, 600-900, 900-1200, 1200-1500x10⁻⁶mm²sec⁻¹ for ADC and 0-0.2, 0.2-0.4, 0.4-0.6, 0.6-0.8, 0.8-0.1min⁻¹ for K^{trans} . #p<0.05, unpaired Student's t-test between vehicle and cediranib-treated cohorts. *p<0.05, paired Student's t-test.

Figure 4. Histological assessment of perfusion and vascular density in intracranial MDA-MB-231 LM2-4 tumors in response to cediranib.

a) Representative fluorescence images of the uptake of the perfusion marker Hoechst 33342 (blue), and immunohistochemical detection of the vascular endothelial marker CD31 (red), acquired from whole brain sections from mice bearing intracranial MDA-MB-231 LM2-4 tumors treated with vehicle or cediranib. Composite Hoechst 33342 and CD31 images acquired at 40x magnification are also shown, demonstrating both co-localisation and mismatch of the vascular markers. Tumor ROIs are shown in green, T denotes tumor region on the composite images. b) Quantification of Hoechst 33342 perfused area, CD31 positive vessel area, and the percentage of vessels perfused. Three sections per tumor were assessed and the mean for each tumor is represented. #p<0.05, unpaired Student's t-test.

Figure 5. Anatomical, diffusion-weighted and dynamic contrast-enhanced MRI of intracranial MDA-MB-231 LM2-4 tumors treated with B20-4.1.1.

a) T₂-weighted MRI images, and associated parametric ADC and K^{trans} maps, from representative intracranial MDA-MB-231 LM2-4 tumors prior to and 48 hours after a single 10mg/kg dose of isotype-matched control antibody Ragweed:1428 (control) or B20-4.1.1, as indicated. b) Quantification of the change in tumor volume over the 48h treatment period, and of K^{trans} and ADC, prior to, and following, treatment with control antibody (n=6) or B20-4.1.1 (n=7). c) Frequency distributions of all tumor ADC and K^{trans} voxels. Distributions were divided into 5 equally sized bins for each dataset, using 0-300, 300-600, 600-900, 900-1200, 1200-1500x10⁻⁶mm²sec⁻¹ for ADC and 0-0.2, 0.2-0.4, 0.4-0.6, 0.6-0.8, 0.8-0.1min⁻¹ for K^{trans} . ##p<0.01, unpaired Student's t-test between control and B20-4.1.1-treated cohorts; *p<0.05, paired Student's t-test.

Figure 6. Histological assessment of vascular perfusion and permeability in intracranial MDA-MB-231 LM2-4 tumors in response to B20-4.1.1.

a) Representative fluorescence images of the uptake of the perfusion marker Hoechst 33342 (blue), and the permeability marker Evans blue (red), acquired from brain sections taken from mice bearing intracranial MDA-MB-231 LM2-4 tumors treated with either isotype-matched control antibody Ragweed:1428 (control, n=4) or B20-4.1.1 (n=4). Tumor ROIs are shown in green. b) Quantification of Hoechst 33342 perfused area and Evans blue positive area. Three sections per tumor were assessed and the mean for each tumor is represented.

Supplementary Figure S1. Schematic of experimental design

Tumor-bearing animals were randomized into experimental groups when bioluminescence signal reached a level representing a tumor volume of ~25mm³. Mean days after implantation

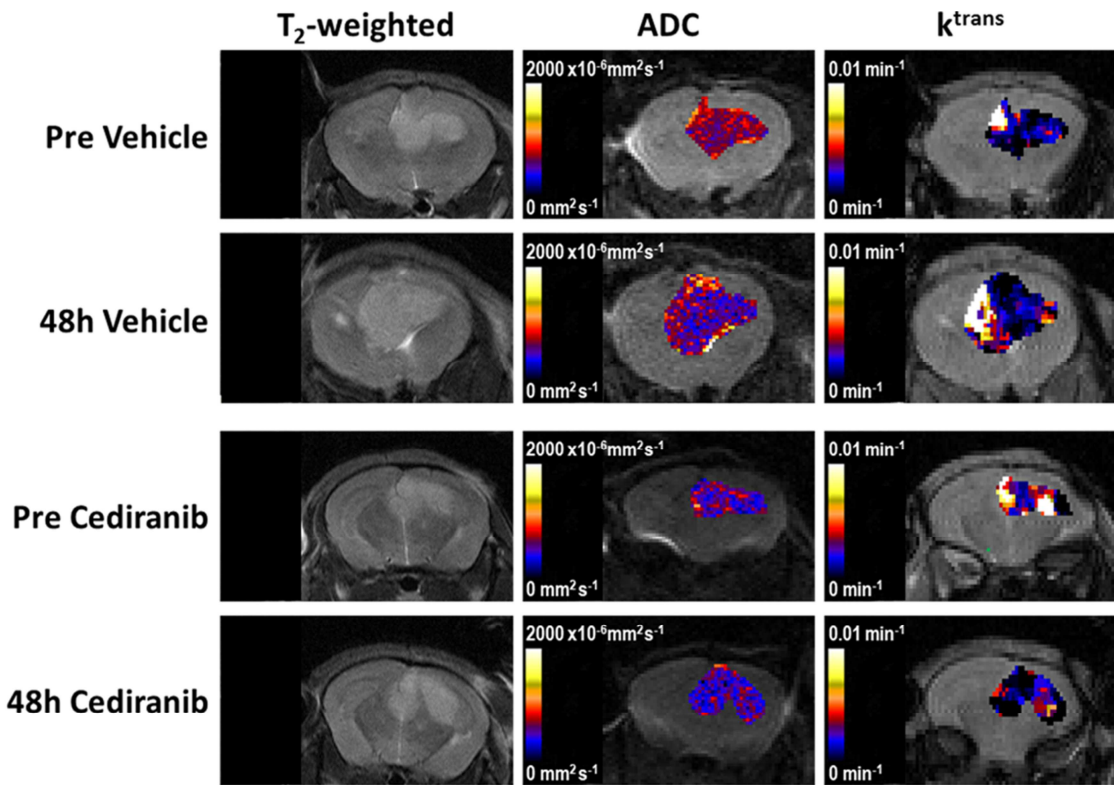
at study start and mean tumor volume (derived from pre-treatment T₂-weighted MRI) ± s.e.m. are shown for each cohort. 6mg/kg cediranib or equivalent volume of vehicle was given daily; a single 10mg/kg dose of B20-4.1.1 or isotype control Ragweed:1428 was given. MRI protocols used diffusion-weighted (DW) and dynamic contrast-enhanced (DCE) MRI or susceptibility-contrast (SC) MRI.

Supplementary Figure S2. Hematoxylin and eosin staining of intracranial SF188^{luc} and MDA-MB-231 LM2-4 tumors.

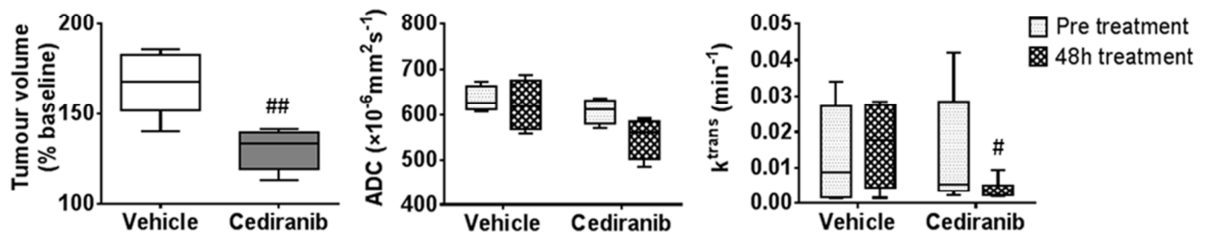
Representative hematoxylin and eosin (H&E) stained 5µm thick formalin-fixed paraffin-embedded (FFPE) brain sections from untreated mice bearing SF188^{luc} or MDA-MB-231 LM2-4 tumors; lower panel x200 magnification. Note the dense cellularity and minimal invasion in the SF188^{luc} tumor, and the invasion associated with the blood vessels (open head arrow) and edema (closed head arrow) present in the MDA-MB-231 LM2-4 tumor.

Figure 1

a



b



c

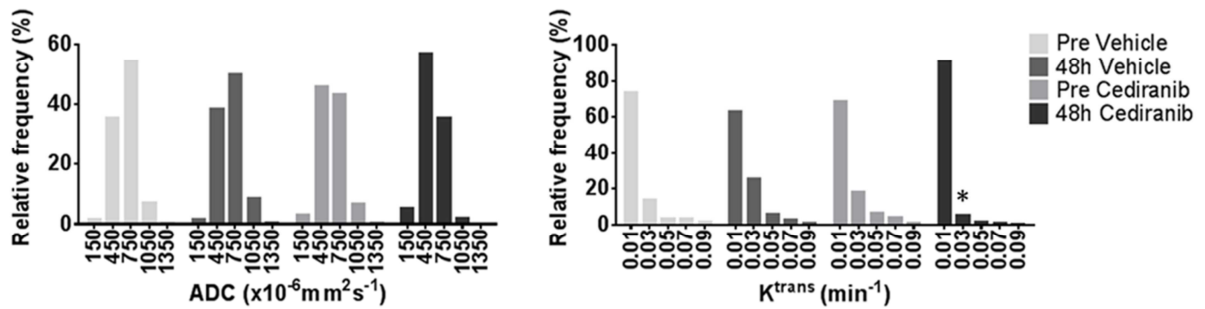
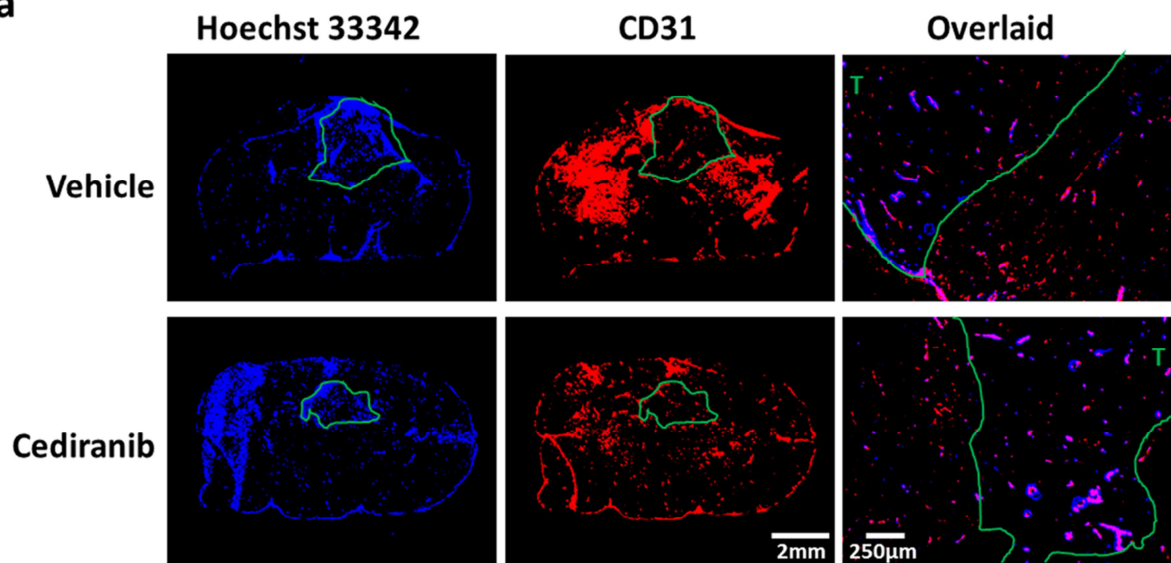


Figure 2

a



b

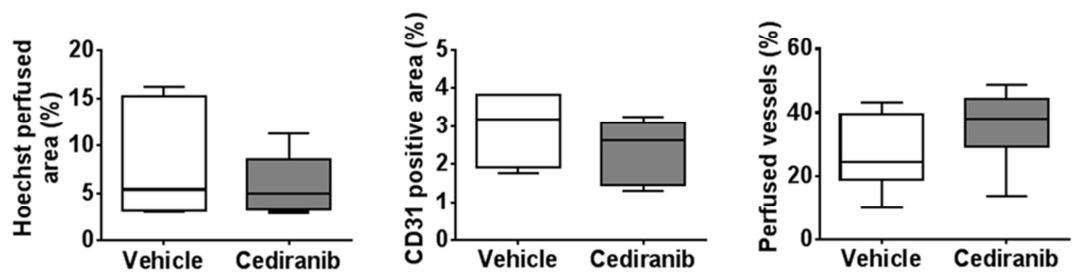
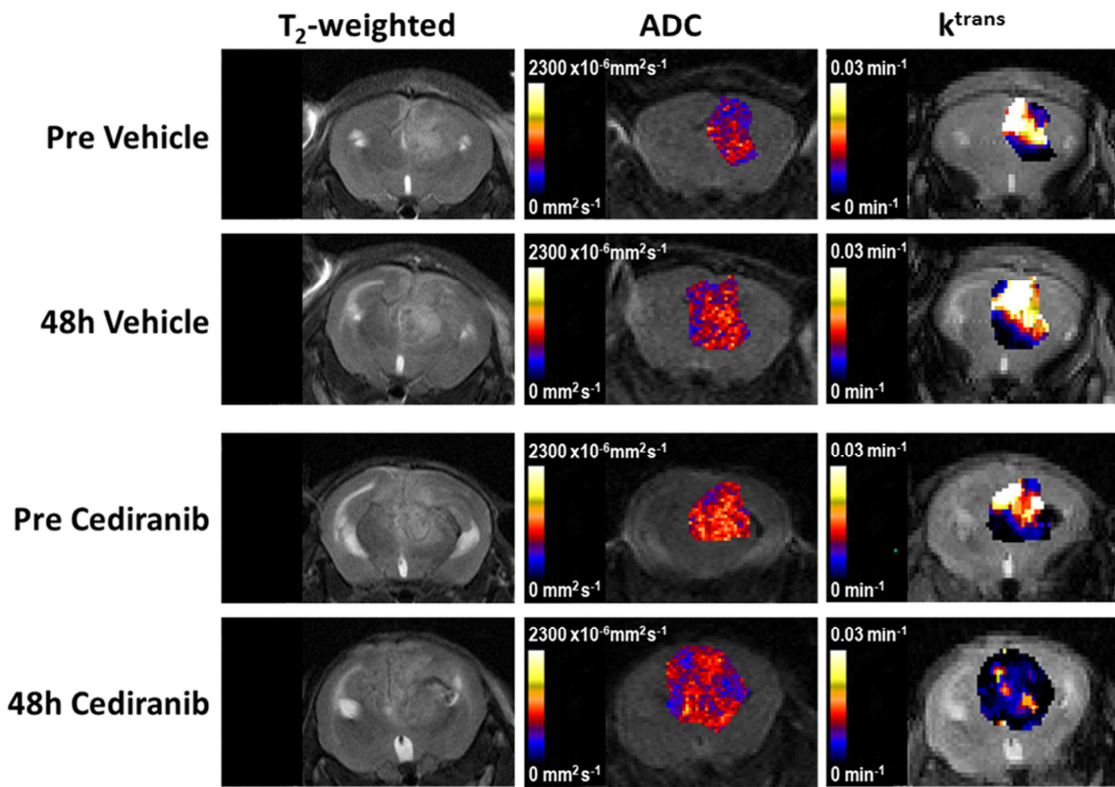
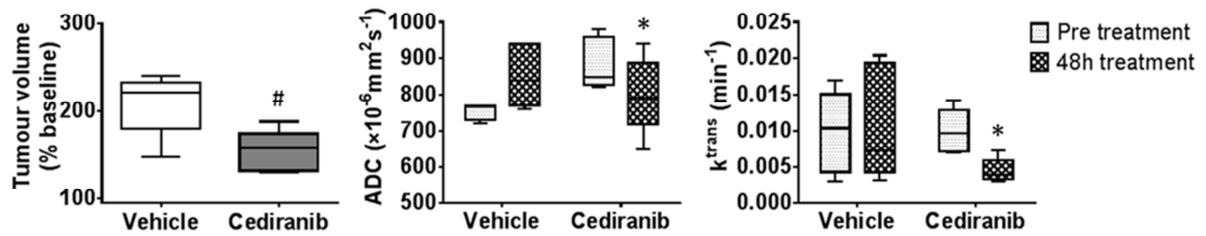


Figure 3

a



b



c

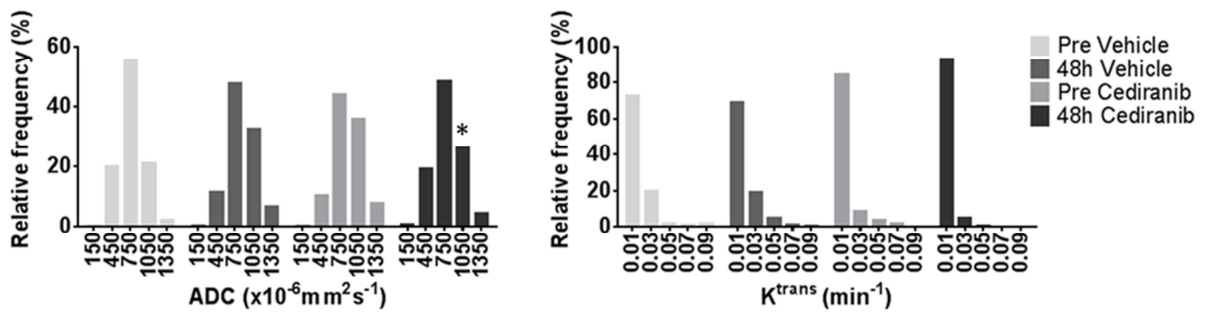
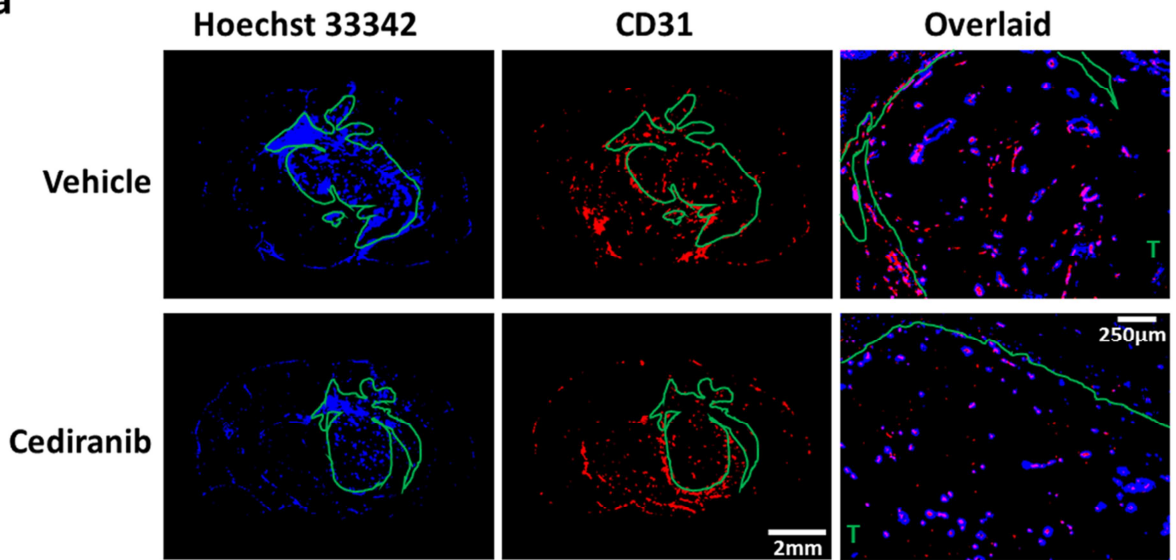


Figure 4

a



b

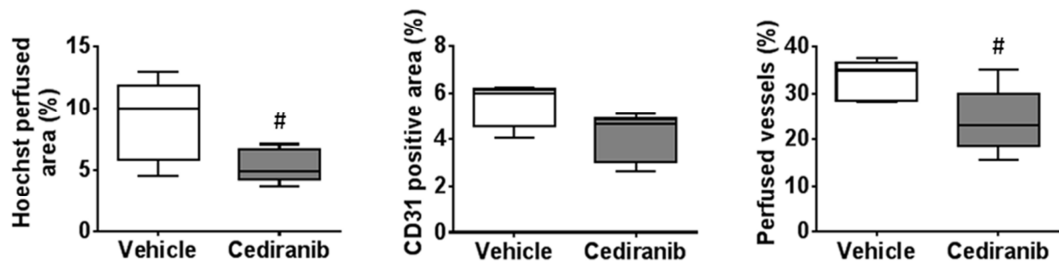
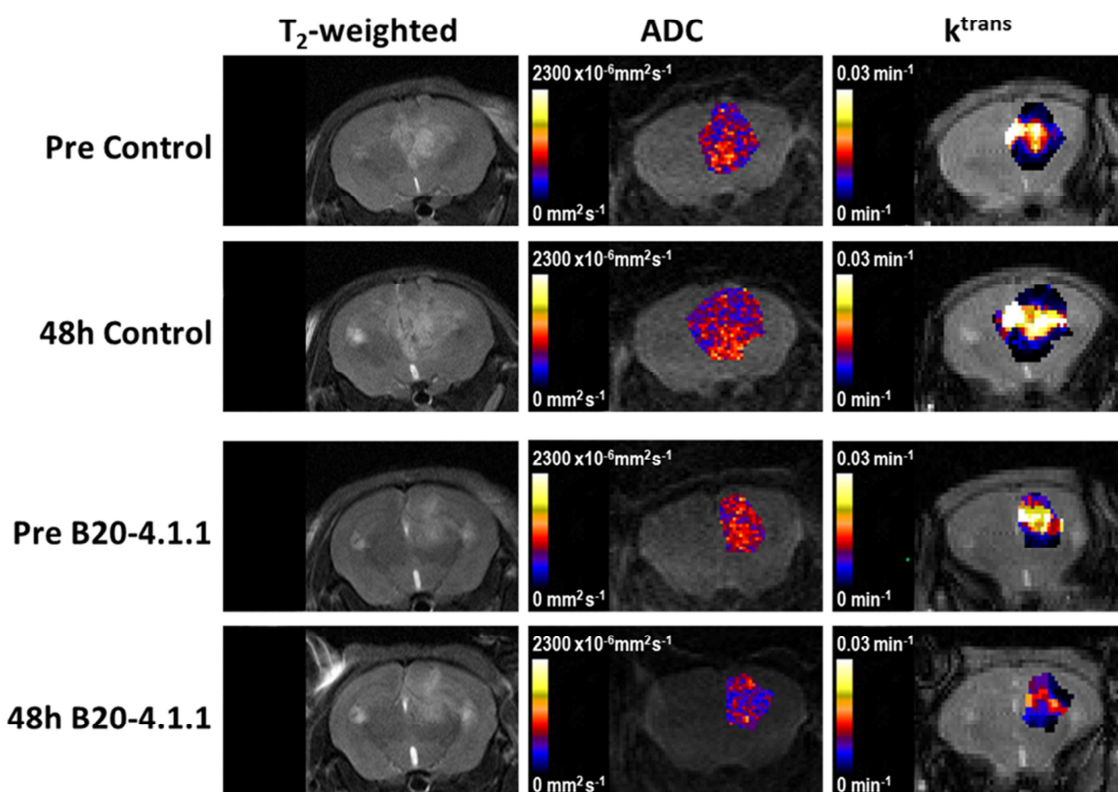
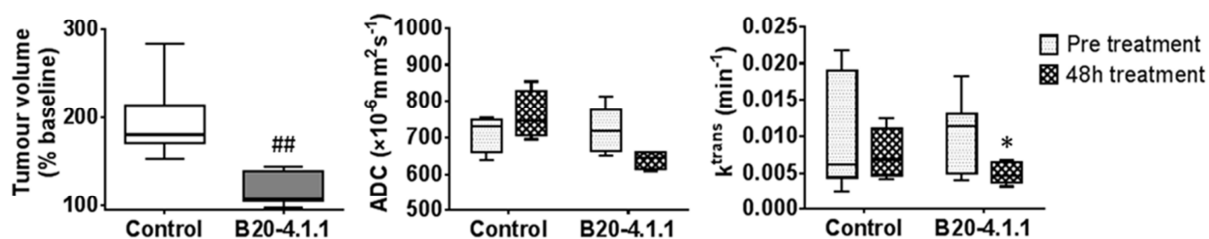


Figure 5

a



b



c

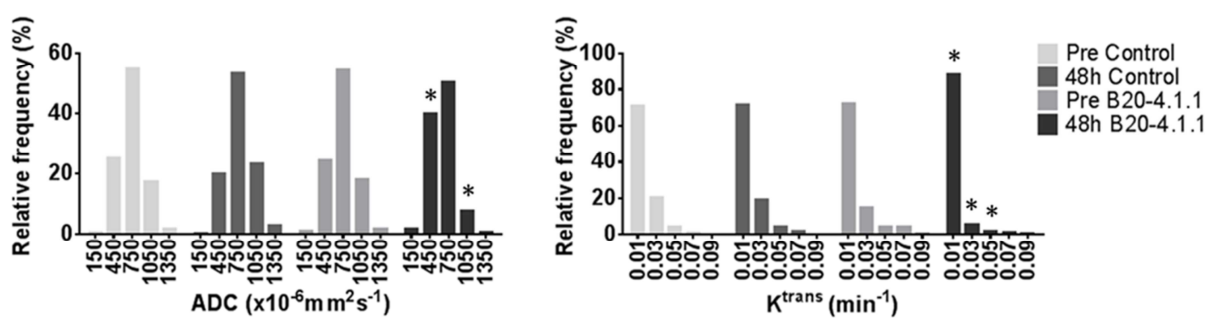
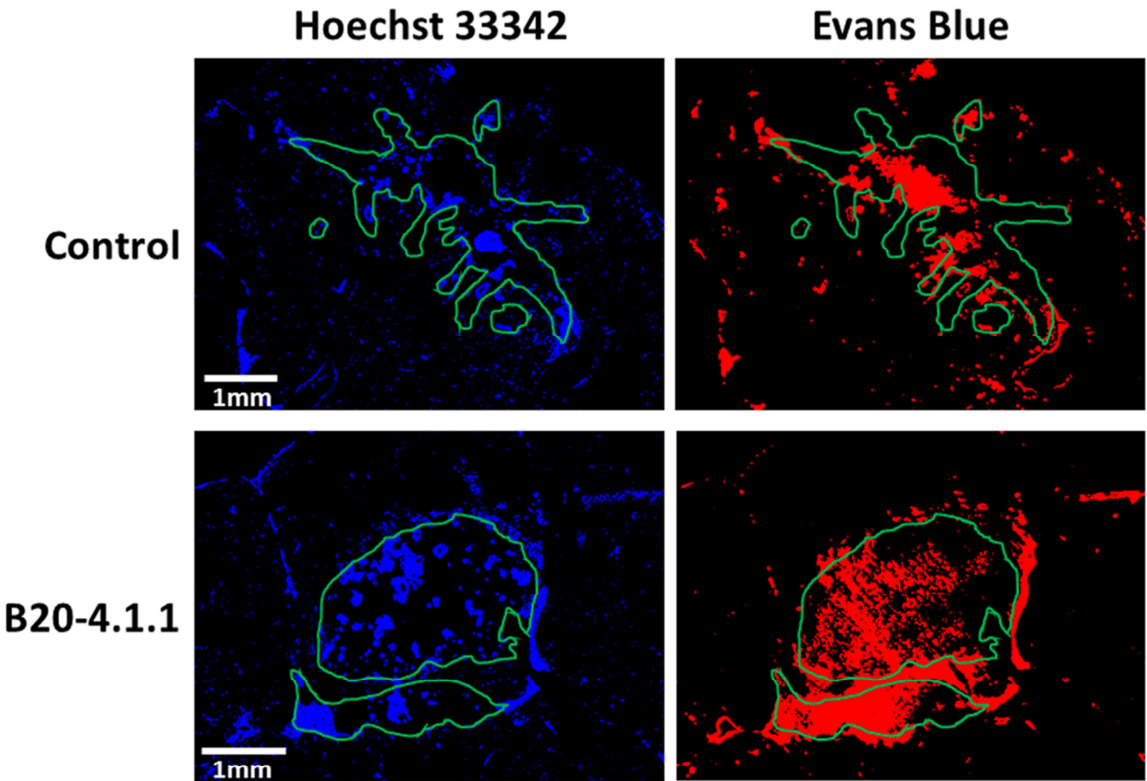
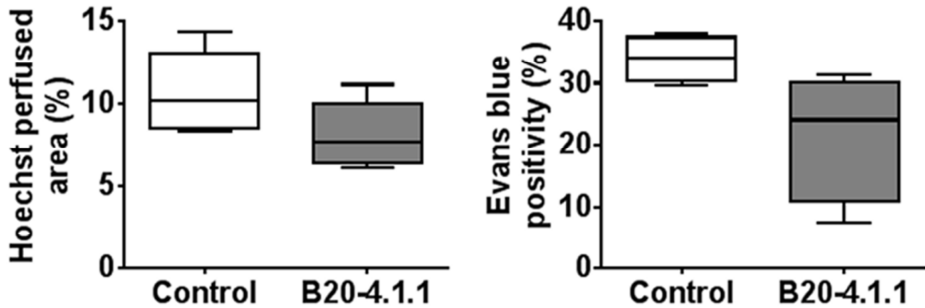


Figure 6

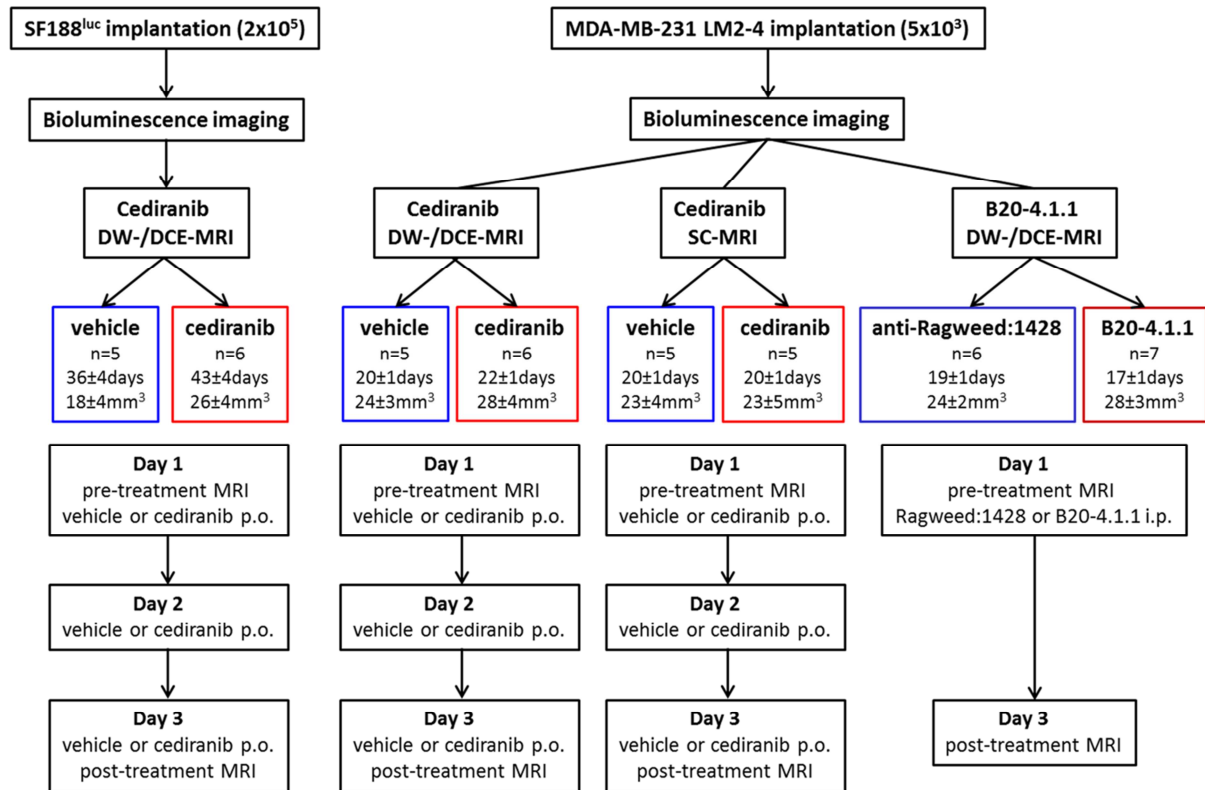
a



b



Supplementary Figure S1



Supplementary Figure S2

